Note Added After First Publication

We regret that for the first publication of this volume on the 1st of November 2023, the placement of the General Discussion sections in the order of the papers was incorrect. The order of these discussion sections has now been corrected. The paper below was affected by the reorder of the volume and, consequently, now displays the new, correct page numbers.

The Royal Society of Chemistry apologises for these errors and any consequent inconvenience to authors and readers.

PAPER

Electrochemical decarboxylation of acetic acid on boron-doped diamond and platinum-functionalised electrodes for pyrolysis-oil treatment†

Talal Ashraf, [ID] [a] Ainoa Paradelo Rodriguez,[a] Bastian Timo Mei [ID] *[ab] and Guido Mul [ID] [a]

Electrochemical decarboxylation of acetic acid on boron-doped-diamond (BDD) electrodes was studied as a possible means to decrease the acidity of pyrolysis oil. It is shown that decarboxylation occurs without the competitive oxygen evolution reaction (OER) on BDD electrodes to form methanol and methyl acetate by consecutive reaction of hydroxyl radicals with acetic acid. The performance is little affected by the applied current density (and associated potential), concentration, and the pH of the solution. At current densities above 50 mA cm^{-2}, faradaic efficiencies (FEs) of 90% towards the decarboxylation products are obtained, confirmed by *in situ* electrochemical mass spectrometry (ECMS) investigation showing only small amounts of oxygen formed by water oxidation. Using platinum-modified BDD electrodes, it is shown that selectivity to ethane, the Kolbe product, strongly depends on the shape and geometry of the platinum particles. Using nano-thorn-like Pt particles, a faradaic efficiency of approx. 40% towards ethane can be obtained, whereas 3D porous platinum nanoparticles showed high selectivity towards the OER. Using thin platinum layers, a high FE of >70% towards ethane was obtained, which is thickness-independent at layer thicknesses above 20 nm. Comparison with other substrates revealed that BDD is an ideal support for Pt functionalisation, giving advantages of stability and high-value-product formation (ethane and methanol). In short, this work provides guidelines for electrode fabrication in the context of the electrochemical upgrading of biomass feedstocks by acid decarboxylation.

Introduction

For a sustainable and circular bioeconomy, biomass has been used as a feedstock for various applications, including production of chemicals and fuels. Pyrolysis

[a]*PhotoCatalytic Synthesis Group (PCS-TNW), University of Twente, Drienerlolaan 5, 7522 NB Enschede, The Netherlands. E-mail: b.t.mei@utwente.nl*

[b]*Industrial Chemistry, Ruhr-Universität Bochum, Universitätsstraße 150, 44801 Bochum, Germany*

† Electronic supplementary information (ESI) available. See DOI: https://doi.org/10.1039/d3fd00066d

oil obtained from the thermochemical conversion of biomass is a low-value biogenic liquid, consisting of carboxylic acids, sugars, phenolics and lignin. Carboxylic acids are a significant fraction of pyrolysis oil with a low energy content (44 MJ kg^{-1}), and their catalytic conversion requires harsh conditions ($\geq$225 °C and 60 bar).[1–3] Electrochemical treatment of pyrolysis oil enables the conversion of carboxylic acids into hydrocarbons by (non-)Kolbe electrolysis. Kolbe chemistry was first reported by Michael Faraday in 1834 and recently gained attention as a potential enabling technology. Thus, product distributions and reaction mechanisms have been analysed.

Electrochemical decarboxylation occurs by the discharge of the deprotonated acid (influenced by the electrolyte pH) at potentials >2.1 V_{NHE}, which is critical for forming alkyl radicals.[4–6] Moreover, mechanistic studies suggest that the coverage of the carboxylate on the electrode surface inhibits the oxygen evolution reaction.[7,8] The reaction proceeds *via* acetate adsorption on the electrode surface followed by a proton-coupled electron transfer (PCET)[7] reaction that results in the formation of carboxyl species (Fig. S1†). The one-electron transfer decarboxylation process produces carbon dioxide as the by-product along with an alkyl radical. Subsequent alkyl-radical conversion depends on the decisive conditions (radical concentration, electrolyte and pH (ref. 9)). Dimerisation results in alkane formation, whereas by disproportionation alkanes and alkenes are formed. The overoxidation of alkyl radicals leads to the formation of carbocations, which deprotonate to form alkenes or react with hydroxyl ions to form alcohols *via* the so-called Hofer–Moest reaction. Moreover, the carbocation can react with the deprotonated acetate to form the respective ester. Several parameters influence the fate and selectivity of (non-)Kolbe electrolysis, such as pH, applied current density, solvent, and electrolyte composition.[5,10]

The electrode material is also crucial, and platinum electrodes have been reported to be ideal for Kolbe electrolysis at negligible water discharge rates. For Pt electrodes, the formation of a barrier layer consisting of carboxylates is suggested to be essential to prevent water oxidation.[9] Electrode materials such as nickel and gold are considered inactive for (non-)Kolbe electrolysis due to the absence of the aforementioned barrier layer. Electrochemical impedance spectroscopy (EIS) has revealed that the pseudo-adsorption capacitance of CH_3COO^- is absent for gold electrodes.[11] Due to an immediate formation of ~30 Å-thick Au_2O_3 (at 0.93 V_{SCE})[11] upon water discharge, the C–C coupling reaction is inhibited. The acetate discharges (~10 Å-thick layer) on Pt–O monolayers (~10 Å)[11] at around 2 V, nearby to the OER region;[12] therefore, Kolbe electrolysis dominates at potentials higher than that of the OER. Carbon-based electrodes show higher activity towards alcohol products, including esters.[5] Thus, the product selectivity of (non-)Kolbe electrolysis is highly dependent on the anode material. Various strategies have been proposed to minimize the use of platinum; among others, platinised electrodes, platinum nanoparticles (NPs) on carbon substrates, nanostructured platinum electrodes, and carbon-based electrodes have been used.[13–16] For Pt-nanoparticle-based electrodes, it has been suggested that the selectivity of the decarboxylation reaction depends on the shape and geometry of the Pt nanoparticles.[15] Yet the activity of platinum-nanoparticle electrodes for (non-)Kolbe electrolysis has to be confirmed[14,17] and the impact of NP loading or the influence of the substrate material has not been fully disclosed. Despite the high activity of platinum electrodes for (non-)Kolbe electrolysis, Pt is prone to dissolving under

(non-)Kolbe conditions, as has been shown by Ranninger et al.[18] In non-aqueous electrolyte, dissolution of approx. 13.3% of a 10 μm-thick Pt electrode was estimated (over a span of one year of electrolysis with a 1 m² electrode), whereas a slightly lower material loss of 8.1% would occur in water-containing electrolytes (Kolbe electrolysis was performed in 1 M acetic acid in ethanol-based solvent at 3 V vs. Fc/Fc⁺).[18]

Boron-doped diamond (BDD) has been used as a substrate material for deposition of metal nanoparticles used in sensing and degradation applications.[19–21] In particular, BDD is widely used due to its inertness towards poisoning within a wide potential window and high stability at high current densities.[22–25] For example, excessive polarisation of BDD for 250 hours in 1 M H_2SO_4 at 1 A cm⁻² resulted in no sign of etching,[26] confirming the stability of BDD. Generally, BDD electrodes show higher corrosion resistance than Pt electrodes under Kolbe electrolysis conditions and thus extended operation can be achieved.[5,27] Still, only a few reports are available related to acetic acid oxidation on BDD,[28] and usually electrooxidation is performed in methanol-, sulphate- or perchlorate-containing electrolytes, while the product distribution is not well described. The decarboxylation of acetic acid on BDD is considered to occur via the formation of weakly adsorbed hydroxyl radicals or other radicals (such as peroxysulphates),[10] which oxidise the acetate, omitting a direct PCET. A direct electron-transfer reaction is only observed for compounds with thermodynamic potentials well below those of water oxidation and formation of OH radicals. For example, formic acid is reported to be fully oxidised to CO_2 via direct electron transfer (DET).[29] Interestingly, BDD is considered unstable at high current densities >50 mA cm⁻² in the presence of alkyl radicals,[30] which produce dangling bonds by abstraction of OH groups from C–OH functional groups. Kashiwada et al.[30] reported that corrosion can be effectively prevented at high pH or moderate current densities. Despite the details known about the reaction mechanism of acetic acid on BDD, the impact of the BDD surface morphology has not yet been considered.[31–33]

In this work, we aim to address the reaction mechanism of (non-)Kolbe/ indirect oxidation of acetic acid in the absence of foreign anion species and explore the stability of BDD during electrolysis in a flow cell. We show that an indirect oxidation occurs in the presence of BDD and moreover we reveal that functionalisation of the BDD surface with thin platinum films or electrodeposited Pt nanoparticles allows tuning of the reaction mechanism towards Kolbe product formation. In comparison to other substrates (graphite, nickel foam and fluorine-doped tin oxide (FTO)), BDD is shown to be an ideal material for functionalisation. In addition, we discuss how the product distribution is affected by current density and pH in a flow cell.

Materials and methods

Acetic acid (glacial, ReagentPlus®, ≥99%, Sigma Aldrich), sulphuric acid (reagent grade, 95–98%, Sigma Aldrich), perchloric acid (reagent grade, 70%, Sigma Aldrich), sodium acetate (ACS reagent, ≥99.0%, Sigma Aldrich), acetone (technical grade, BOOM B.V.), isopropanol (technical grade, BOOM B.V.) and ethanol (technical grade, BOOM B.V.) were used. Hexachloroplatinic acid, potassium tetrachloroplatinate(II) and potassium hexachloroplatinate(IV) were acquired from

Sigma Aldrich. Acetic acid was chosen as a model compound due to its abundancy in pyrolysis oil.[34]

Boron-doped-diamond electrodes (DIACHEM®), with a coating thickness of 15 nm BDD on 2 mm-thick tantalum substrates and a doping level of 2000–5000 ppm of boron incorporated into the diamond lattice, were acquired from CONDIAS Gmbh. The procedure for manufacturing the electrodes is reported in detail elsewhere.[35] Surface cleaning prior to electrochemical testing was performed by washing with Milli-Q water (18.2 MΩ cm) and isopropanol, prior to ultrasonication in Milli-Q water for 10 minutes, anodic polarisation in 1 M $HClO_4$ for 30 minutes and subsequent rinsing with Milli-Q water, following a protocol reported in the literature.[36] For comparison, graphite (LFYGY Industry Materials Professional Supplier, China), FTO (redox.me, Sweden) and nickel foam (IKA, Germany) electrodes were used as both electrodes and substrates. Prior to use, the graphite was polished with carbide paper and sonicated for 10 minutes in Milli-Q water. Impurities were removed electrochemically in 1 M H_2SO_4 by potential cycling in between 0.2–1 V_{RHE} at 50 mV s^{-1} for 100 cycles. The FTO electrodes were cleaned in an ultrasonic bath in acetone, isopropanol, ethanol and Milli-Q water for 15 minutes each. The nickel foam was cleaned by ultrasonication in 2 M HCl solution for 10 minutes prior to ultrasonication in ethanol and Milli-Q water for five minutes each.

Thin platinum layers (5, 20, 50 and 100 nm) were deposited on cleaned BDD substrates using a sputtering system (AJA International, USA). Electrodeposition of Pt nanoparticles was carried out with different platinum salt solutions. Porous nanoflower-like platinum nanoparticles were electrodeposited from a solution of 8 mM H_2PtCl_6 in 0.5 M H_2SO_4 by applying a constant potential of −0.24 $V_{Ag/AgCl}$ for 15 minutes, and are denoted as ED-A hereafter. Dispersed platinum nanoparticles were obtained from a solution of 1 mM K_2PtCl_4 in 0.5 M H_2SO_4 during a constant potential treatment (−1 $V_{Ag/AgCl}$ for 200 seconds), and labelled as ED-B. Thorn-like platinum nanoparticles (active-crystal-plane particles grown on 2D substrates[37,38]) were produced in 2.5 mM H_2PtCl_6 in 0.5 M H_2SO_4 at −0.2 $V_{Ag/AgCl}$ for 15 minutes, and labelled as ED-C. Platinum nanocrystals were produced by applying −0.22 $V_{Ag/AgCl}$ for 15 minutes using a solution of 4.0 mM K_2PtCl_6 in 0.5 M H_2SO_4, and labelled as ED-D.

The electrochemical decarboxylation reactions were performed in 1 M acetate solution at pH 5 (acetic acid/sodium acetate). BDD, graphite, FTO, NiF (bare), Pt-sputtered BDD, and Pt nanoparticles on BDD were used as working electrodes. Platinised titanium (Magneto Special Anodes B.V.) and Ag/AgCl (3 M NaCl, ProSense) were used as counter and reference electrodes, respectively. Electrolysis was performed in a custom-made glass cell at a constant stirring rate of 600 rpm with a helium (99.99%) purge of 30 mL min^{-1}. Prior to batch electrolysis, the electrochemical cell and electrode holders were thoroughly rinsed with ethanol, washed five times with Milli-Q water and subsequently boiled in Milli-Q water. Gas analysis during the reaction was performed by online gas chromatography (GC). A flame ionisation detector (FID) and an RTX-1 column (15 m × 0.32 mm I.D., 5 μm fused silica film thickness at 45 °C) were used for detection of hydrocarbons. CO_2, O_2 and H_2 were detected with a thermal conductivity detector (TCD) coupled with a Carboxen® 1010 column (15 m × 0.32 mm I.D. at 70 °C). External calibration was conducted for CH_4, C_2H_4, C_2H_6, H_2, O_2, and CO_2 with r^2 (coefficient of determination) > 0.995. Hofer–Moest and other liquid products

(methanol and methyl acetate) were detected by liquid analysis. Aliquots were collected from the electrolyte, diluted 10 times with water, neutralised and detected using a headspace GC-FID (Agilent) using a Zebron 7HG-G013-11 column (0.25 μm I.D., 250 μm × 40 m) for product separation.

Cyclic voltammetry (CV) in the potential range of 0.05–1.2 V_{RHE} was performed in 1 M H_2SO_4 solution to determine the electrochemically active surface area (ECSA) of the platinised electrodes. CV was also performed in 1 M acetic acid/sodium acetate solution (0–3 V_{RHE}) before and after electrolysis, followed by current interruption (CI) for *iR* (ohmic drop) correction. Chronopotentiometry was performed at 25 mA cm^{-2} at room temperature and pressure, and the measured potentials were converted to RHE scale. The calculations for faradaic efficiency (FE) are explained in the ESI.† Flow experiments were conducted using the commercial Condias Synthesis cell kit (see Fig. S2†).

Electrochemical mass spectrometry (ECMS, instrument from Spectro Inlets, Copenhagen, Denmark) was performed for instantaneous detection of volatile products. In particular, signals related to methane, ethane, ethylene, methanol, methyl acetate, oxygen and CO_2 were recorded during cyclic voltammetry in 1 M acetic acid/sodium acetate electrolyte. A platinum mesh and an Ag/AgCl electrode (sat. KCl, CH Instruments) were used as the counter and reference electrodes, respectively. The morphology and surface structure of the platinum nanoparticles and BDD electrodes were visualised using scanning electron microscopy (SEM) performed with a ZEISS MERLIN HR-SEM or a JEOL JSM 7610F, respectively. The stability of the BDD electrodes was analysed by SEM and using a custom-made Raman spectroscopy setup equipped with a 650 nm laser, before and after electrolysis. Due to the surface morphology and uneven BDD crystal height, three measurements were taken at different depth levels from the surface to inside of the sample. The scanned area is 10 × 10 μm and measurements were performed at 35 mW, for 150 ms at 50 kHz. The Raman spectrometer is equipped with an optical microscope (BX41 Olympus, objective Olympus 40× NA 0.95).

Results and discussion

(Non-)Kolbe electrolysis at various electrodes

Kolbe electrolysis of acetic acid/sodium acetate at pH 5 was performed at 25 mA cm^{-2} using BDD, graphite, FTO and nickel foam as working electrodes. Fig. 1a shows the cyclic voltammograms obtained in acetate solution. Clearly, the lowest onset potential and the highest oxidative currents (39 mA cm^{-2} at 3 V_{RHE}) are achieved with nickel foam (NiF), which is primarily due to its characteristic high surface area. The onset potential of 1.8 V_{RHE} is related to the oxygen evolution reaction (OER) as also confirmed by the high faradaic efficiency for oxygen obtained during electrolysis (Fig. 1b). For BDD, the CV resembles previously reported data in the literature,[39] and only above 2.5 V_{RHE} is an exponential increase in currents observed. The CV obtained with FTO electrodes closely resembles that obtained with BDD, but the increase in current is less steep (attaining 5.7 mA cm^{-2} at 3 V_{RHE}). Similarly, for graphite electrodes, the oxidation current density at high potential is low (5.7 mA cm^{-2} at 3 V_{RHE}), contrasting with its early current onset. The product selectivities, as shown by the faradaic efficiencies in Fig. 1b, are clearly electrode-material specific. Kolbe electrolysis products are not observed for NiF electrodes. With a very high FE towards oxygen of up to 95%,
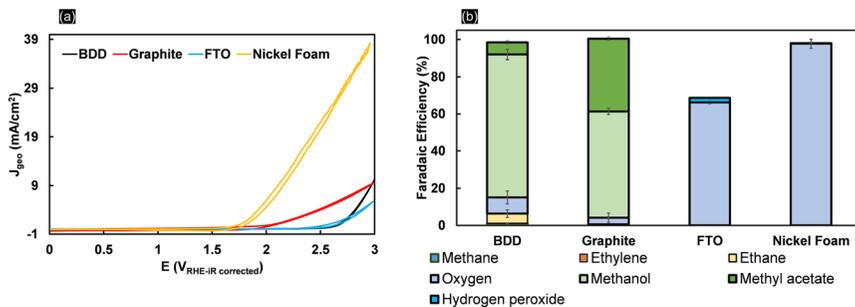
Fig. 1 Effect of different electrodes on (non-)Kolbe electrolysis: (a) CV of BDD, graphite, FTO and nickel foam conducted in 1 M acetic acid/sodium acetate at pH 5; (b) average FE towards (non-)Kolbe/Hofer–Moest/indirect oxidation products during electrolysis of 1 M acetic acid/sodium acetate for 50 minutes in a batch cell at 25 mA cm^{-2} and pH 5.

formation of oxides on the nickel surface favours the OER[40] (Fig. S3†). When using FTO, the OER is also dominant and only small quantities of H_2O_2 were detected, besides oxygen, resulting in a faradaic efficiency of 2%. Considering that acetic acid oxidation on FTO and nickel foam is inhibited, both materials are inadequate electrode materials for (non-)Kolbe electrolysis. Formation of methanol and methyl acetate in equivalent FEs is achieved at graphite electrodes. Thus, over-oxidation of the methyl radical to the carbocation leads to Hofer–Moest product formation.[5] During chronopotentiometry (Fig. S4†), the rise in potential within the electrolysis time frame (50 minutes) observed for graphite and FTO electrodes suggests that both materials exhibit instability under (non-)Kolbe electrolysis conditions. The instability of FTO was reflected in the working electrode potential reaching ~ 7 V_{RHE}. This contrasts with the high stability observed for BDD, where the electrode potential was stable at 3.6 V_{RHE} (Fig. S4†). Furthermore, when employing BDD electrodes, the electrooxidation of acetic acid is more selective to methanol as compared to graphite electrodes. Considering that the separation of azeotropic methanol and methyl acetate mixtures is challenging, the oxidation on BDD can be considered more efficient.[41]

The stability of BDD electrodes during Kolbe electrolysis was analysed by Raman spectroscopy (Fig. S5†) and SEM (Fig. S6†). The BDD coatings were investigated before and after Kolbe electrolysis as shown in Fig. 2. The Raman spectra are dominated by bands at 488, 1137, 1216, 1323, and 1147 and 1550 cm^{-1}, in agreement with literature reports.[42,43] The spectra were taken across random areas on the BDD surface and averaged for analysis (Fig. S5†). The Raman spectrum of the as-received BDD electrode confirms a high boron doping, as in general with increasing boron concentration in the diamond lattice the first-order diamond phonon line[44] shifts from 1332 cm^{-1} to lower wavenumber. Comparison of the BDD surface before and after electrolysis reveals a slight change in the signal of the diamond phonon mode, which shifts from 1312 cm^{-1} to 1323 cm^{-1} after electrolysis. In addition, the scattering intensity at 488 cm^{-1} and 1216 cm^{-1} decreases, corresponding to the weak band due to metallic and non-metallic impurities. Considering that the signal at 488 cm^{-1} is due to the boron doping level and vibration modes of boron clusters and pairs,[19,42] Raman analysis suggests that the concentration of boron in the diamond lattice decreases with
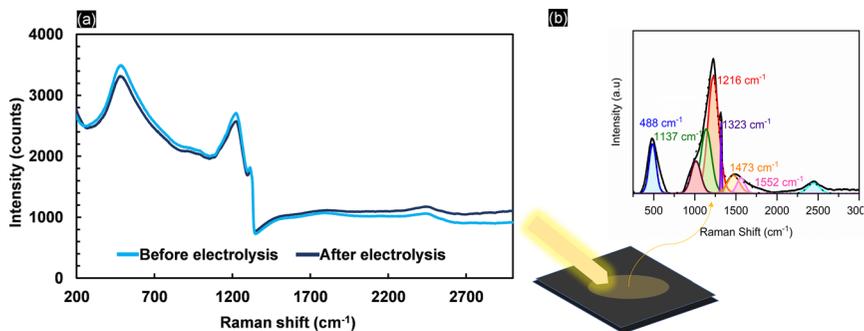
Fig. 2 (a) Raman spectra of BDD before and after 2 h electrolysis in 1 M acetic acid/sodium acetate pH 5 at 25 mA cm^{-2}. The BDD electrodes used have a concentration of 2000–5000 ppm boron atoms in the lattice. (b) Deconvoluted Raman spectra of BDD reveal the positions of the bands, in accordance with the existing literature.

electrolysis. Degradation of BDD can occur by either boron leaching or the graphitization of carbon at the grain boundaries. The G-band peak observed at 1552 cm^{-1} is due to the bond stretching of sp^2 carbon atoms in rings and chains and is in agreement with the literature.[45] The band present at 1473 cm^{-1} corresponds to the sp^2 carbon of *trans*-polyacetylene lying in the grain boundaries. Interestingly, due to the high quality of the BDD coating, polymeric carbon species[46] are not prominent before electrolysis as highlighted by the minor signal intensities at 1470 cm^{-1}. Still, it is worth noting that the post-treatment (chronopotentiometery at 25 mA cm^{-2} for 30 minutes in 1 M HClO$_4$) (see Materials and methods) removed graphitized carbon effectively (Fig. S6c†). Overall, Raman analysis confirmed that the electrolytic corrosion on BDD is negligible during acetic acid electrolysis at low current densities. Therefore, we conducted all subsequent experiments below 100 mA cm^{-2}. The amount of boron content (within a cubic centimetre) can roughly be estimated by an empirical relationship[47] (eqn (1)).

$$[B] = 8.44 \times 10^{30} \times \exp(-0.048 \times W) \ (cm^{-3}). \tag{1}$$

W is the wavenumber corresponding to the peak of the Lorentzian component of the Raman spectra at 400–600 cm^{-1}. The estimated concentration of boron doping in the BDD electrode is found to be 5.66 × 10^{20} cm^3.

We further explored the impact of electrolysis conditions (pH and current density) on the electrooxidation using a divided flow cell (compartment separation was achieved using a Nafion 324 cation exchange membrane, see Fig. S2†) and an acetic acid/sodium acetate solution as both catholyte and anolyte. The results are shown in Fig. 3. The FE is relatively independent of the pH and current density. Methanol is the dominant product, while the consecutive reaction to methyl acetate is most pronounced at low current densities and moderate pH values (pH 5). Under constant-flow conditions (60 mL min^{-1}), the highest accumulative FE towards methanol was achieved at 100 mA cm^{-2}. The high selectivity towards methanol is attributed to the high concentration of weakly adsorbed OH
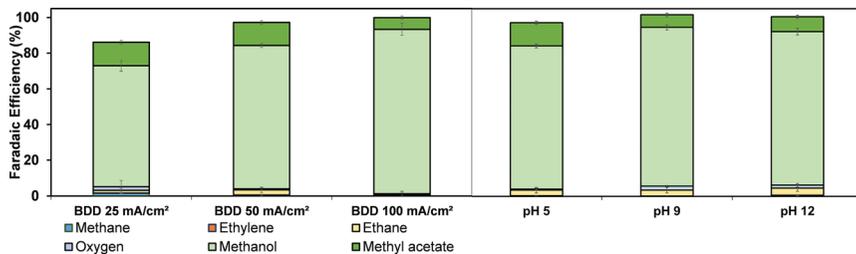
Fig. 3 The effect of current density (left) on the electrooxidation of 1 M acetic acid/sodium acetate on BDD in a flow cell at pH 5 and the pH effect (right) on FE towards methanol and methyl acetate at 50 mA cm^{-2} in a flow cell at 60 mL min^{-1} (catholyte and anolyte flow).

radicals, which promote oxidation of concentrated acetic acid/sodium acetate to methanol.

When decreasing the concentration of acetic acid to 0.5 M, the FE towards methanol remains dominant (Fig. S7†). Thus, the oxidation is not limited by the hydroxyl radical concentration or autoinhibition[39] at 0.5 M acetic acid concentration. Interestingly, in earlier reports, methyl acetate was not detected during acetic acid oxidation on BDD electrodes,[28] so here we report the full product distribution of acetic acid oxidation at BDD electrodes under different conditions for the first time.

Platinised electrodes

To alter the selectivity from the formation of methanol to Kolbe electrolysis, *i.e.*, ethane formation, and to investigate the behaviour of the Pt thin films and nanoparticles on a well-characterized and stable substrate, BDD was functionalised with thin platinum layers by sputtering (5, 20, 50 and 100 nm Pt) and Pt nanoparticles by electrodeposition. For thin film samples, the ECSA normalized to the mass deposited (m^2 g$_{pt}^{-1}$) was obtained by integration of the H$_{upd}$ (hydrogen underpotential deposition) region from the CVs, assuming a monolayer hydrogen charge of 210 μC cm$_{Pt}^{-2}$ (Fig. S8b†). The ECSA normalized to the loading of the amount of platinum deposited decreases in order of increasing platinum layer thickness (Fig. S8c†). This is in contrast to the behaviour observed for platinum nanoparticles (Fig. S16†), but in agreement with the literature.[48] Importantly, the inhomogeneous BDD might influence the nucleation and film growth,[49] likely leading to a non-uniform coating of the substrate. Indeed, non-normalized ECSA data revealed that the surface area (cm^2) and roughness factor increase from the 5 nm sputtered layers up to the 20 nm thin films and only small differences are observed for thick coatings (Fig. S9b and c†).

To investigate the potential-dependent product distribution of the Kolbe electrolysis of acetic acid/sodium acetate solution in real-time, an ECMS investigation was performed with BDD and platinised BDD (5 nm sputtered Pt) electrodes. ECMS is a modern technology compared to conventional DEMS (differential electrochemical mass spectroscopy), as discussed in ESI section 27.† The mass spectrometry data recorded during the CV are shown in Fig. 4. Generally, the transient (*m/z*) signals confirm the presence of (non-)Kolbe products.
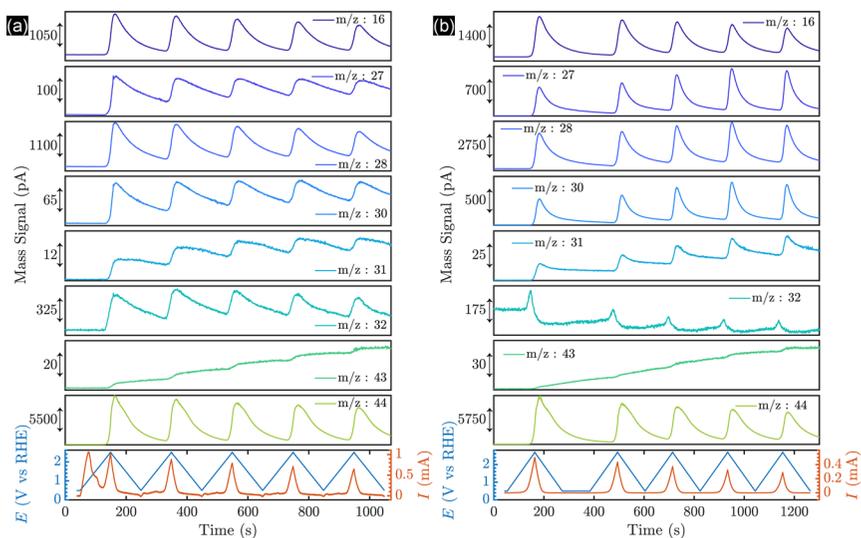
Fig. 4 Electrochemical mass spectrometry (ECMS) measurement of Kolbe electrolysis and indirect oxidation using (a) BDD and (b) platinised BDD electrodes. Cyclic voltammetry has been performed in 1 M acetic acid/sodium acetate at pH 5 in both cases. The recorded signals correspond to methane ($m/z = 16$), ethane ($m/z = 27$ and 30), ethylene ($m/z = 27$ and 28), the by-product CO_2 ($m/z = 44$), the competitive reaction product O_2 ($m/z = 32$) and the indirect oxidation/Hofer–Moest products methanol ($m/z = 31$) and methyl acetate ($m/z = 43$).

As shown in Fig. 4a, the onset of the OER for bare BDD is observed at 2.136 V_{RHE}. Considering that for BDD electrodes the onset of the OER is usually observed at potentials >2.3 V,[50] it is speculated that oxygen evolution proceeds *via* decomposition of hydrogen peroxide produced by OH radical recombination, as depicted in eqn (2)–(4).

$$H_2O \xrightarrow{+H,-e} {}^{\bullet}OH \tag{2}$$

$${}^{\bullet}OH + {}^{\bullet}OH \rightarrow H_2O_2 \tag{3}$$

$$2H_2O_2 \rightarrow O_2 + 2H_2O \tag{4}$$

Subsequently, decarboxylation products are detected. Methanol and methyl acetate are accumulated in the liquid phase during cyclic voltammetry, due to their low vapor pressure. Compared to the signal intensities of CO_2, the main Kolbe product, ethane, is only observed in minor amounts, in agreement with the above presented batch and flow cell experiments. Importantly, here we reveal that the onset of the decarboxylation reaction and oxygen evolution and the transient product signals are similar.

This is in contrast to the thin-film-coated Pt/BDD electrodes (Fig. 4b), for which oxygen evolution and the decarboxylation reaction are well-separated in potential. The onset potential for the OER is 1.98 V_{RHE} on Pt/BDD, and only at potentials >2.1 V_{RHE} are Kolbe and indirect oxidation products detected.

Importantly, at the onset of Kolbe product formation, the OER is inhibited, being in strong contrast to the profiles observed for bare BDD. In addition, oxygen evolution is decreasing during successive cycling, while Kolbe-product formation is more pronounced, as revealed by the intensity of ethane ($m/z = 30$). Thus, likely a barrier layer builds up[7] during successive cycling, enabling a shift in selectivity towards Kolbe products. Finally, it is apparent that Kolbe products are primarily produced on Pt/BDD, as revealed by the higher currents of the respective signals. Nevertheless, the presence of the methanol and methyl acetate suggests that the BDD surface is not fully covered with Pt and exposed BDD facets enable OH formation and alcohol and ester formation.

Constant-current electrolysis of acetic acid was subsequently performed at 25 mA cm^{-2} using a variable thickness of Pt (Fig. 5). For 5 nm Pt on BDD electrodes, initially a high selectivity towards OER is observed and only during extended polarisation is product formation transitioning to the Kolbe product formation (Fig. S11†). This is likely due to the formation of (110) and (100) facets of Pt (Fig. S9a†), which are not present during the CV recorded before electrolysis. After 50 minutes of constant polarisation, the selectivity of the reaction for the 5 nm-thick Pt film shifted primarily to ethane, but is still limited to a FE of ~59% (Fig. S10†). CVs recorded in 1 M acetic acid/sodium acetate show the presence of an inflection zone at 2.5 V_{RHE} for 20, 50 and 100 nm Pt layers, and the peak oxidation current of 33.5 mA cm^{-2} was achieved with a 5 nm Pt layer. The absence of an inflection zone for the 5 nm Pt layer shows the dominancy of the OER, which is also displayed in the product distribution, where up to 80% faradaic efficiency reflects the selectivity of the reaction towards the OER as the electrolysis starts.
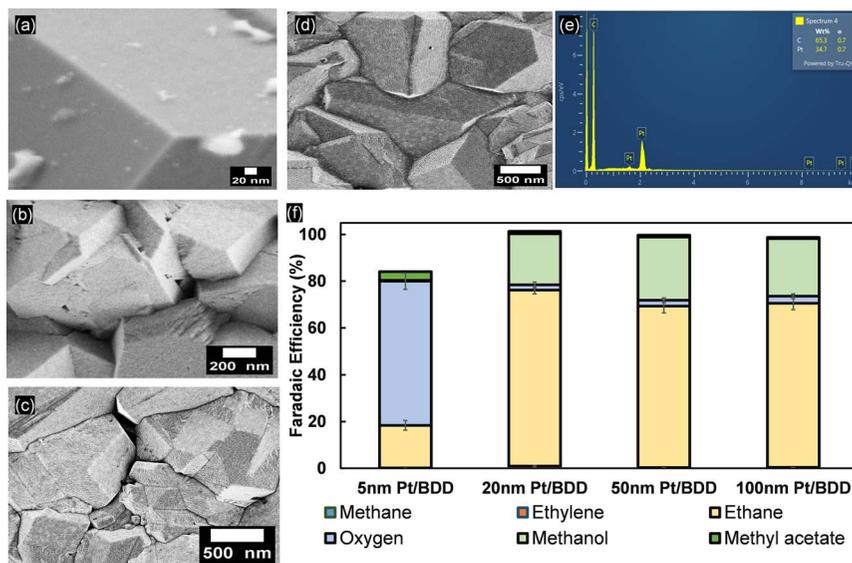

Fig. 5 SEM images of Pt-sputtered BDD electrodes: (a) 5 nm, (b) 20 nm, (c) 50 nm and (d) 100 nm Pt; (e) EDX of 20 nm Pt/BDD showing the presence of Pt and carbon from diamond; (f) averaged FE towards (non-)Kolbe electrolysis with different platinum-layer thicknesses on BDD, obtained during electrolysis at 25 mA cm^{-2} in 1 M acetic acid/sodium acetate (pH 5).

For all other electrodes, *i.e.* with Pt films >20 nm, instantaneous Kolbe-product formation is observed at FE >70% (Fig. S11c†). This is still lower than that obtained for Pt foil, where an FE towards ethane formation of ~90% is reproducibly observed (Fig. S12†). Simultaneously, methyl acetate is detected, allowing the electron balance to be closed. Thus, it appears that methyl radical recombination is still less favourable for BDD-supported Pt, likely due to an insufficient surface radical concentration. Instead, the exposed BDD surface (see Fig. S13†) allows for formation of methanol (Fig. 5f). Likely, some uncovered BDD surface is maintained, in between BDD crystals as suggested by SEM analysis (Fig. 5).

Considering the interesting product formation transients observed for 5 nm Pt on BDD, and in an attempt to study lower Pt loadings, BDD was functionalised with Pt nanoparticles obtained by electrodeposition (see Materials and methods).

The electrodeposited mass of Pt on the BDD is variable due to different deposition times and applied potentials. The FE and production rate of the products of each type of electrodeposited nanoparticle on the BDD were compared to evaluate the selectivity towards Kolbe electrolysis. For porous platinum nanoflowers (ED-A; for SEM see Fig. 6a), an average FE toward ethane of
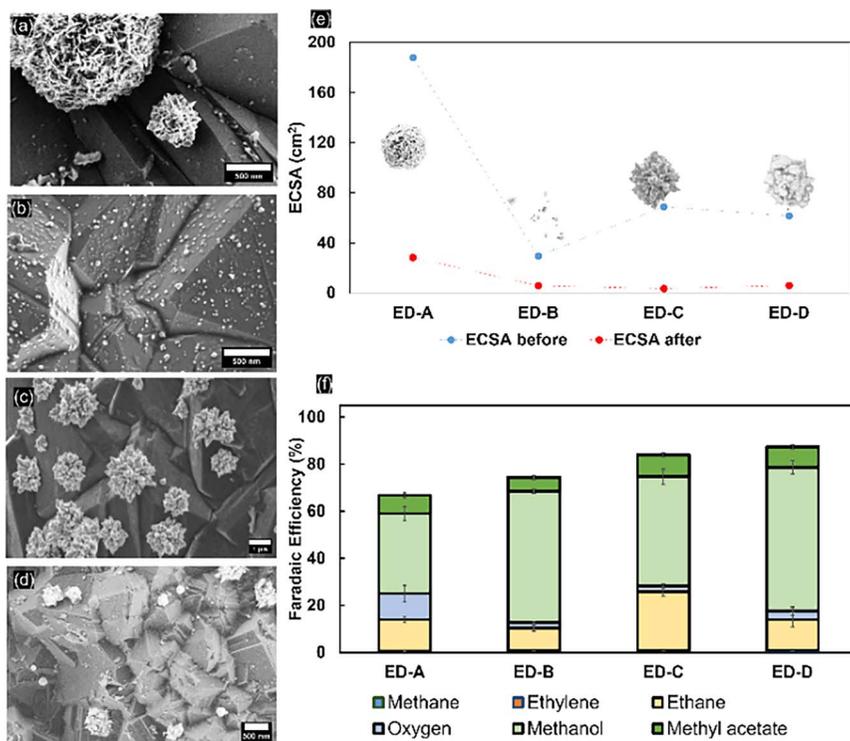

Fig. 6 SEM images of Pt electrodeposition on BDD electrodes: (a) ED-A nanoflowers, (b) ED-B dispersed nanoparticles, (c) ED-C nano-thorns, and (d) ED-D nanocrystals; (e) ECSA (cm^2) in 1 M H$_2$SO$_4$ before and after (non-)Kolbe electrolysis; (f) average FE towards (non-)Kolbe electrolysis/indirect oxidation products from different geometries of platinum nanoparticles on BDD at 25 mA cm^{-2} in 1 M acetic acid/sodium acetate (pH 5). The electron balance was not closed, which could be due to the formation of H$_2$O$_2$ or other side products (not detected).

around 14% (±1.134) was obtained. Initially, the OER dominated with faradaic efficiencies up to 50% (Fig. S17†). Nevertheless, during extended electrolysis, the OER becomes negligible, similar to the trends observed for 5 nm Pt thin films. Post-electrolysis liquid analysis revealed that methanol and methyl acetate were obtained at faradaic efficiencies of 33% ± 2.9 and 7.8% ± 1.0, respectively. For freestanding, well-dispersed platinum nanoparticles (ED-B; for SEM see Fig. 6b), the FE towards Kolbe products (9.2% ± 1.5) is low throughout the electrolysis. The OER is suppressed but the FE towards methanol (55.7% ± 1.8) shows that, despite the coverage, the dispersed nanoparticles are not highly selective for Kolbe electrolysis and instead the decarboxylation reaction predominantly occurs at the BDD substrate. With platinum nano-thorns (ED-C; for SEM see Fig. 6c), an ethane selectivity of up to 43% ± 1.9 was observed, similar to the reported high selectivity towards Kolbe electrolysis when deposited on carbon fibre paper.[14] With extended electrolysis time, the FE decreased to 20% and remained stable. In agreement with the high Kolbe-product selectivity, low FEs towards methanol and methyl acetate (46.4% and 9.4%, respectively) were observed. Finally, the lowest Kolbe-product selectivity was observed for platinum nanocrystals (ED-D; for SEM see Fig. 6d). Clearly, the structure and shape of the Pt particles is of high relevance for Kolbe electrolysis or OER activity, as revealed by the high selectivity towards the OER on Pt nanoflower structures (ED-A). For ED-A electrodes, a mass-normalised ECSA of 12.4 $m_{Pt}^2\ g_{Pt}^{-1}$ and roughness factor of 35.4 were determined. Considering that for ED-C a similar mass-normalized ECSA (13.7 $m_{Pt}^2\ g_{Pt}^{-1}$) at a significantly lower roughness factor (11.6) has been determined, and that for ED-C samples the electrochemical surface area and roughness factor are 5.31 $m^2_{Pt}\ g_{Pt}^{-1}$ and 5.6, respectively, it is likely that a high selectivity for Kolbe products is achieved for a fine-balance of the Pt-surface-to-volume ratio and abundance of low-coordinated Pt sites that contribute to an enhanced electrocatalytic activity.[51] To support this hypothesis, BDD modified with platinum nanoflowers was prepared using even higher Pt loadings. Therefore, ED-A electrodeposition was carried out for 30 minutes, which results in a fully covered surface without any exposed BDD facets (Fig. S18a†). The determined ECSA increased to 21.5% at a roughness factor of 60.5, being stable after electrolysis. Here, OER is the predominant reaction (FE 97%, Fig. S19†).

Eliminating the effect of the substrate, the complete inhomogeneous coverage fails to promote Kolbe electrolysis due to exceedingly high roughness factors and porosity, which omits formation of a homogenous acetate barrier layer. It also proves that for promoting the Kolbe reaction, flat surfaces are more favourable. Finally, it is important to note that the loss in activity observed during Kolbe electrolysis is independent of the precise shape of the platinum nanoparticles. This is also in agreement with the ECSA data obtained before and after electrolysis (Fig. 6e) that reveal a loss of 80–90% of nanoparticles during electrolysis. Stabilisation of Pt nanoparticles might be achieved by selective modification of the (111) facets of BDD, as reported in the literature.[52] Facet-selective modification will be evaluated in ongoing research.

To disclose the importance of the substrate used for Pt nanoparticle deposition, electrodeposition of nanoflower-like Pt particles (ED-A) has been repeated on different substrates (graphite, FTO and nickel foam). The particles retain the same shape when deposited on graphite and FTO substrates, but differences in surface coverage were noticeable (Fig. 7a–d). On NiF, the same electrodeposition
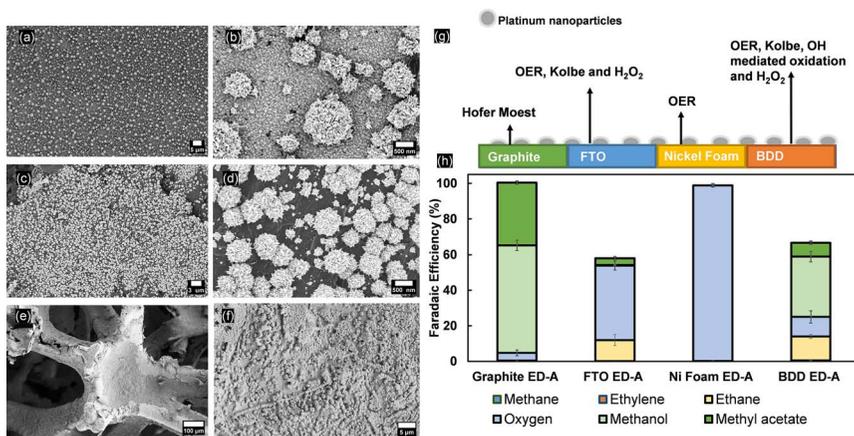
Fig. 7   SEM images of Pt nanoflowers electrodeposited on different substrate electrodes: (a and b) FTO, (c and d) graphite, and (e and f) nickel foam; (g) illustration of predominant reactions on platinum nanoparticles on different substrates; (h) average FE towards (non-)Kolbe electrolysis on platinum nanoflower particles with different substrates at 25 mA cm^{-2} in 1 M acetic acid/sodium acetate (pH 5).

method resulted in the formation of a Pt layer, as confirmed by the EDX analysis shown in Fig. S20†. Kolbe electrolysis performed under the same conditions as used for the Pt/BDD samples revealed that only for the Pt/FTO electrodes was (non-)Kolbe product formation observed (Fig. 7g). As shown above, bare FTO samples are inactive for Kolbe electrolysis, yet after Pt-nanoparticle deposition, ethane was detected at a FE of up to 11% at the expense of the OER. Moreover, traces of H_2O_2 were detected. For Pt-modified graphite electrodes, the product distribution is also slightly influenced by the presence of Pt and the OER was increased to 5% at similar methanol and methyl acetate formation rates. This shows that the exposed surface of the substrate is greatly influencing the selectivity of Kolbe electrolysis. Finally, Pt was not effectively influencing the efficiency and the OER was taking place exclusively. In comparison with bulk platinum electrodes, not only is the tailoring of selectivity towards (non-)Kolbe electrolysis greatly affected by the size, shape or facets of the nanoparticles, but also the substrate is greatly influencing the reaction that is predominantly occurring. Therefore, it is important to find a correlation between the coverage of platinum nanoparticles, their shape, and the substrate to design an electrode that efficiently promotes Kolbe electrolysis.

Conclusions

(Non-)Kolbe/indirect oxidation was performed on platinum and BDD electrodes in 1 M acetic acid/sodium acetate at pH 5. It is shown that BDD can be used as a standalone electrode for alcohol and ester production from carboxylic acids, or as an ideal substrate for surface functionalization. The decarboxylation reaction on bare BDD is OH-radical mediated, and results in methanol, methyl acetate and ethane production as shown by ECMS. The reaction is slightly limited by the concentration of acetic acid and autoinhibition for concentrated electrolytes

(above 1 M acetic acid solution). The reaction selectivity can be shifted by tuning the surface of the BDD with a thin layer of platinum or by using electrodeposited platinum nanoparticles. For thicker Pt layers (>20 nm), the reaction is highly selective to Kolbe products and less selective to indirect oxidation products. The use of nanoparticles can alter the selectivity towards (non-)Kolbe electrolysis, but low faradaic efficiencies are still retained, which decrease over time. The complex shapes and structures of platinum nanoparticles are decisive factors for their stability on the substrate and selectivity towards Kolbe electrolysis. Other electrode substrates (FTO, Ni and graphite) are not suitable for the extreme conditions necessary, and generally promote side reactions instead of Kolbe electrolysis.

Author contributions

Talal Ashraf: conceptualization, methodology, experimentation, data analysis and writing. Bastian Timo Mei: conceptualization, methodology, supervision, data analysis, writing and reviewing. Ainoa Paradelo Rodriguez: EC-MS experiments and discussions. Guido Mul: supervision, reviewing and editing.

Conflicts of interest

There are no conflicts to declare.

Acknowledgements

References

1 I. G. O. Črnivec, P. Djinović, B. Erjavec and A. Pintar, *RSC Adv.*, 2015, **5**, 54085–54089.
2 A. Ong, J. Pironon, P. Robert, J. Dubessy, M.-C. Caumon, A. Randi, O. Chailan and J.-P. Girard, *Geofluids*, 2013, **13**, 298–304.
3 R. V. Shende and J. Levec, *Ind. Eng. Chem. Res.*, 1999, **38**, 3830–3837.
4 C. Stang and F. Harnisch, *ChemSusChem*, 2016, **9**, 50–60.
5 F. J. Holzhäuser, J. B. Mensah and R. Palkovits, *Green Chem.*, 2020, **22**, 286–301.
6 E. Klocke, A. Matzeit, M. Gockeln and H. J. Schäfer, *Chem. Ber.*, 1993, **126**, 1623–1630.
7 S. Liu, N. Govindarajan, H. Prats and K. Chan, *Chem Catal.*, 2022, **2**, 1100–1113.
8 A. K. Vijh and B. E. Conway, *Chem. Rev.*, 1967, **67**, 623–664.
9 I. Markó and F. Chellé, in *Encyclopedia of Applied Electrochemistry*, ed. G. Kreysa, K. Ota and R. F. Savinell, Springer, New York, NY, 2014, pp. 1151–1159.

10 M. O. Nordkamp, B. Mei, R. Venderbosch and G. Mul, *ChemCatChem*, 2022, **14**, e202200438.

11 I. Sekine and H. Ohkawa, *Bull. Chem. Soc. Jpn.*, 1979, **52**, 2853–2857.

12 Z. Yu, *Int. J. Electrochem. Sci.*, 2021, 210240.

13 Y. Qiu, J. A. Lopez-Ruiz, G. Zhu, M. H. Engelhard, O. Y. Gutiérrez and J. D. Holladay, *Appl. Catal., B*, 2022, **305**, 121060.

14 G. Yuan, L. Wang, X. Zhang, R. Luque and Q. Wang, *ACS Sustainable Chem. Eng.*, 2019, **7**, 18061–18066.

15 G. Yuan, C. Wu, G. Zeng, X. Niu, G. Shen, L. Wang, X. Zhang, R. Luque and Q. Wang, *ChemCatChem*, 2020, **12**, 642–648.

16 Y. Peng, Y. Ning, X. Ma, Y. Zhu, S. Yang, B. Su, K. Liu and L. Jiang, *Adv. Funct. Mater.*, 2018, **28**, 1800712.

17 S. Xu, X. Niu, G. Yuan, Z. Wang, S. Zhu, X. Li, Y. Han, R. Zhao and Q. Wang, *ACS Sustainable Chem. Eng.*, 2021, **9**, 5288–5297.

18 J. Ranninger, P. Nikolaienko, K. J. J. Mayrhofer and B. B. Berkes, *Chemsuschem*, 2022, **15**, e202102228.

19 T. Zhang, Z. Xue, Y. Xie, G. Huang and G. Peng, *RSC Adv.*, 2022, **12**, 26580–26587.

20 B. Zribi and E. Scorsone, in *Proceedings of Eurosensors 2017*, MDPI, Paris, France, 2017, p. 452.

21 X. Lyu, J. Hu, J. S. Foord, C. Lou and W. Zhang, *J. Mater. Eng. Perform.*, 2015, **24**, 1031–1037.

22 X. Du, Z. Mo, Z. Li, W. Zhang, Y. Luo, J. Nie, Z. Wang and H. Liang, *Environ.Int.*, 2021, **146**, 106291.

23 J. M. Freitas, T. da C. Oliveira, R. A. A. Munoz and E. M. Richter, *Front. Chem.*, 2019, **7**, 190.

24 Y. Tian, X. Chen, C. Shang and G. Chen, *J. Electrochem. Soc.*, 2006, **153**, J80.

25 K. Wenderich, B. A. M. Nieuweweme, G. Mul and B. T. Mei, *ACS Sustainable Chem. Eng.*, 2021, **9**, 7803–7812.

26 M. Panizza, G. Siné, I. Duo, L. Ouattara and Ch. Comninellis, *Electrochem. Solid-State Lett.*, 2003, **6**, D17.

27 J. D. Wadhawan, F. J. Del Campo, R. G. Compton, J. S. Foord, F. Marken, S. D. Bull, S. G. Davies, D. J. Walton and S. Ryley, *J. Electroanal. Chem.*, 2001, **507**, 135–143.

28 A. Arts, M. T. de Groot and J. van der Schaaf, *Chem. Eng. J. Adv.*, 2021, **6**, 100093.

29 A. Kapałka, B. Lanova, H. Baltruschat, G. Fóti and C. Comninellis, *J. Electrochem. Soc.*, 2009, **156**, E149.

30 T. Kashiwada, T. Watanabe, Y. Ootani, Y. Tateyama and Y. Einaga, *ACS Appl. Mater. Interfaces*, 2016, **8**, 28299–28305.

31 N. Kurig, J. Meyers, F. J. Holzhäuser, S. Palkovits and R. Palkovits, *ACS Sustainable Chem. Eng.*, 2021, **9**, 1229–1234.

32 K. Arai, K. Watts and T. Wirth, *ChemistryOpen*, 2014, **3**, 23–28.

33 D. E. Collin, A. A. Folgueiras-Amador, D. Pletcher, M. E. Light, B. Linclau and R. C. D. Brown, *Chem.–Eur. J.*, 2020, **26**, 374–378.

34 G. Lyu, S. Wu and H. Zhang, *Front. Energy Res.*, 2015, **3**, 28.

35 M. Fryda, Th. Matthée, S. Mulcahy, A. Hampel, L. Schäfer and I. Tröster, *Diamond Relat. Mater.*, 2003, **12**, 1950–1956.

36 T. L. Read and J. V. Macpherson, *J. Visualized Exp.*, 2016, 53484.

37 W. Zhang, L. Zhang, G. Zhang, P. Xiao, Y. Huang, M. Qiang and T. Chen, *New J. Chem.*, 2019, **43**, 6063–6068.

38 P. R. Sajanlal, T. S. Sreeprasad, A. K. Samal and T. Pradeep, *Nano Rev.*, 2011, **2**, 5883.

39 A. Kapałka, G. Fóti and C. Comninellis, *J. Electrochem. Soc.*, 2008, **155**, E27.

40 M. Steimecke, G. Seiffarth, C. Schneemann, F. Oehler, S. Förster and M. Bron, *ACS Catal.*, 2020, **10**, 3595–3603.

41 Z. Zhang, Q. Zhang, G. Li, M. Liu and J. Gao, *Chin. J. Chem. Eng.*, 2016, **24**, 1584–1599.

42 N. Wächter, C. Munson, R. Jarošová, I. Berkun, T. Hogan, R. C. Rocha-Filho and G. M. Swain, *ACS Appl. Mater. Interfaces*, 2016, **8**, 28325–28337.

43 N. Dubrovinskaia, L. Dubrovinsky, N. Miyajima, F. Langenhorst, W. A. Crichton and H. F. Braun, *Z. Naturforsch. B*, 2006, **61**, 1561–1565.

44 J. V. Macpherson, *Phys. Chem. Chem. Phys.*, 2015, **17**, 2935–2949.

45 J. Xu, Y. Yokota, R. A. Wong, Y. Kim and Y. Einaga, *J. Am. Chem. Soc.*, 2020, **142**, 2310–2316.

46 A. C. Ferrari and J. Robertson, *Phys. Rev. B: Condens. Matter Mater. Phys.*, 2001, **63**, 121405.

47 Y. Chen, X. Gao, G. Liu, R. Zhu, W. Yang, Z. Li, F. Liu, K. Zhou, Z. Yu, Q. Wei and L. Ma, *Funct. Diam.*, 2021, **1**, 197–204.

48 S. Taylor, E. Fabbri, P. Levecque, T. J. Schmidt and O. Conrad, *Electrocatalysis*, 2016, **7**, 287–296.

49 P. Schmitt, V. Beladiya, N. Felde, P. Paul, F. Otto, T. Fritz, A. Tünnermann and A. V. Szeghalmi, *Coatings*, 2021, **11**, 173.

50 A. Kapałka, H. Baltruschat and C. Comninellis, in *Synthetic Diamond Films*, John Wiley & Sons, Ltd, 2011, pp. 237–260.

51 Y. Yang, M. Luo, W. Zhang, Y. Sun, X. Chen and S. Guo, *Chem*, 2018, **4**, 2054–2083.

52 I. González-González, E. R. Fachini, M. A. Scibioh, D. A. Tryk, M. Tague, H. D. Abruña and C. R. Cabrera, *Langmuir*, 2009, **25**, 10329–10336.